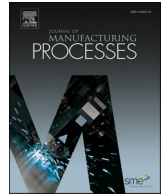




Contents lists available at ScienceDirect

Journal of Manufacturing Processes

journal homepage: www.elsevier.com/locate/manpro

Laser scan strategy descriptor for defect prognosis in metal additive manufacturing using neural networks

Kahraman Demir^a, Zhizhou Zhang^a, Adi Ben-Artzy^b, Peter Hosemann^c, Grace X. Gu^{a,*}

^a Department of Mechanical Engineering, University of California, Berkeley, CA 94720, USA

^b Ben-Gurion University, POB. 653, Beer-Sheva, 84105, Israel

^c Department of Nuclear Engineering, University of California, Berkeley, CA 94720, USA

ARTICLE INFO

Keywords:

Additive manufacturing
Residual stress
Laser scan strategies
Machine learning
Computational modeling

ABSTRACT

In situ and post-print defects, including excessive residual stresses and poor microstructural properties, are important concerns in the part design and setup stages of powder bed fusion (PBF) manufactured parts. Laser scan strategies are well known to be correlated with the development of these defects; however, due to the lack of complex scan strategy descriptors and the consequential imposition of simple scan strategies, these correlations are not well understood and are difficult to investigate. This work proposes a methodology for an intuitive quantitative descriptor of scan strategies that has the potential to provide quick prognoses to predict defects. To demonstrate this, a neural network is trained to accurately predict post-print residual stress distributions using the descriptor of a specified path. It is envisioned that this descriptor could allow for the circumvention of current costly prevention mechanisms and increase confidence and reliability in metal additive manufacturing technologies.

1. Introduction

Additive manufacturing has established itself as an essential set of manufacturing technologies for the making of incredibly complex parts which is critical to contemporary design goals [1–9]. In particular, metal additive manufacturing (mAM) is defined as the group of manufacturing technologies with which metal parts are manufactured in a layer by layer fashion. Among the many different mAM technologies, powder bed fusion (PBF) is the most common in which a concentrated heat source, usually a laser or electron beam, melts thin spread powder in precise locations layer by layer. This fuses the powder together at local regions creating a 3D component. Following PBF in popularity is directed energy deposition, which also involves a moving heat source where material is transported to the point where the heat source is focused on. In this instance the part is created freeform and the heating and cooling history of a component strongly depend on the geometry of the component and the heat source path.

A shared challenge among AM techniques involving moving heat sources is the selection of a scan strategy. The selection of scan strategy involves the selection of a path and speed with which a heat source moves over the powder to consolidate a cross-sectional layer [10,11]. While melting a powder layer, underlying layers also heat up and

usually re-melt. This leads to multiple local heat treatments which in turn can lead to various defects. The cooling rate of the consolidated layer is also a contributor to defect development [12]. Naively planning scan strategies can lead to critical defects in printed parts including high porosity, poor microstructural properties, bad surface quality, and excessive warping. It is non-trivial to consider all possible defect mechanisms when planning scan strategies, and worse still is the lack of reliably interpretable correlations between scan strategies and defect mechanisms. A lot of scan strategies deployed today are derived from trial-and-error approaches.

The literature contains numerous experimental studies empirically demonstrating the dependency of part properties to scan strategies. Using scanning electron microscopy imagery and image processing techniques, Arisoy et al. demonstrated that PBF process parameters including laser power, scan velocity, hatch distance, and scan strategy were correlated with cooling rates, thermal gradients, and microstructural properties [13]. Through x-ray computed tomography, microscopic imaging and other techniques, Rashid et al. demonstrated that there are correlations between scan strategies and the porosity, hardness, and microstructural properties of printed parts [14]. Levkulich et al. investigated the correlations between various process parameters and the residual stresses in titanium alloy PBF parts using x-ray

* Corresponding author.

E-mail address: ggu@berkeley.edu (G.X. Gu).

<https://doi.org/10.1016/j.jmpro.2021.05.011>

Received 5 February 2021; Received in revised form 28 April 2021; Accepted 7 May 2021

Available online 21 May 2021

1526-6125/© 2021 The Society of Manufacturing Engineers. Published by Elsevier Ltd. All rights reserved.

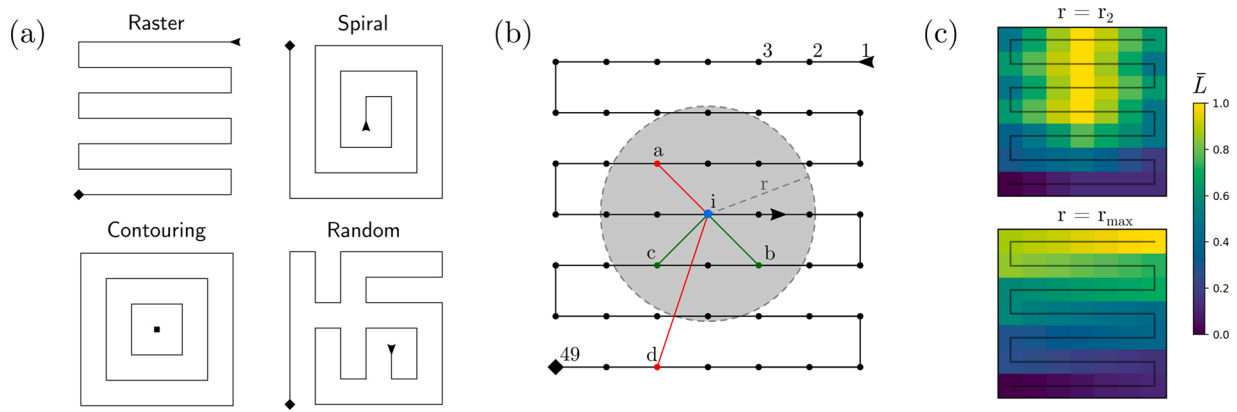


Fig. 1. (a) Different types of possible paths including a random one. (b) Illustration of RSP quantification. Green and red lines depict nonzero and zero relative spacetime differences respectively. (c) Normed RSP maps of the same path in (b) with different radii of influence. (For interpretation of the references to colour in this figure legend, the reader is referred to the web version of this article).

diffraction, hole-drilling, and contour method techniques and concluded that there are measurable correlations [15]. Lee et al. used in situ near-infrared imaging and computational modeling to reveal dependencies between part geometry, scan strategies, cracking and residual stresses. Additionally, they proposed scan strategies that could potentially mitigate cracking and warping [16].

It should be noted that challenges associated with the accuracy of experimental measurements and computational models pose difficulties in investigating correlations between process parameters and print properties. It is possible that this difficulty is exacerbated by the limited parameters imposed on scan strategies due to the a priori adoption of simple strategies such as raster or spiral scanning as shown in our schematic in Fig. 1(a). For example, in the case of the simple back and forth raster, line spacing and raster angle (the angle between the scan lines and the consolidated surface) are the only parameters needed to describe the scan strategy (excluding parameters associated with the consolidated areas geometrical constraints), whereas it is nontrivial to describe an irregular path without rigorously listing the laser’s velocity at certain times which requires a relatively significant amount of interpretive effort, even for the short and somewhat structured *random* path in Fig. 1(a).

In this paper, we introduce a method for quantitatively describing laser scan strategies which can be used to draw correlations between it and post-print properties. In order to demonstrate its validity and applicability, thermomechanical simulations are performed with random laser strategies and used in tandem with the descriptor to train a machine learning model to predict post-print mechanical properties using the strategy descriptor. Neural networks (NNs) are utilized to provide a measure of the detected correlations between the descriptor and post-print properties which in turn gives insight on the descriptor’s ability to communicate a scan strategy’s spatiotemporal properties.

2. The descriptor: The Relative Spacetime Proximity (RSP) map

One of the main causal links between print properties and scan strategies is the spatiotemporal temperature distribution of the consolidated surface. Simply, areas on the surface where the laser more frequently visits may be generally hotter than areas that are less frequently visited. This idea is the driving force behind the descriptor proposed in this work, named the Relative Spacetime Proximity (RSP) map. The RSP map quantifies the spatiotemporal proximity of points on the laser path with spatial and temporal criteria. An RSP map obtained through evaluating the cumulative spacetime proximity (\tilde{L}_i) for all n nodes on a path where,

$$\tilde{L}_i = \sum_j^n L(x_i, x_j), \quad L(x_i, x_j) = \begin{cases} e^{-\gamma \sqrt{r_{ij}^2 + x_{ij}^2}}, & t_{ij} > 0 \text{ and } x_{ij} < r \\ 0, & \text{otherwise} \end{cases} \quad (1)$$

where $x_{ij} = |x_i - x_j|_2$ and $t_{ij} = t_i - t_j$

t_{ij} and x_{ij} are the time difference and distance, respectively, between path nodes i and j . L essentially evaluates the spacetime distance ($\sqrt{\gamma t_{ij}^2 + x_{ij}^2}$) between two path nodes with a time difference coefficient of $\gamma > 0$ to adjust for temporal significance. \tilde{L}_i is the summation of spacetime differences between the i th node and every other node. The spacetime difference, L , is zero when the time difference is nonpositive and when the relative distance is greater than the radius r , named here the *radius of influence*.

The reasoning for imposing the radius of influence is that points on the consolidated surface that are far apart are not expected to thermally influence one another as those that are closer together. The time criterion enforcing positivity is used to capture only the effect of nodes revisiting chronologically preceding nodes and not those that proceed. In other words, points on a surface that are already consolidated will not significantly thermally influence points on the surface that are yet to be consolidated. The motivation for this kind of quantification is to capture the notion of reheating due to the heat source revisiting areas. Fig. 1(b) exemplifies the mechanism of the equation by depicting both nonzero and zero spacetime differences with green and red colors respectively on a simple raster path.

After evaluating \tilde{L}_i for every node, the values are scaled (\bar{L}_i) and stored in a vector variable \bar{L} shown in Eq. (2). This quantification leads to the RSP map shown in Fig. 1(c) in its spatial form for two different radii of r are used.

$$\bar{L}_i = \frac{\tilde{L}_i}{\max_{1 < k < n} \tilde{L}_k}, \quad \bar{L} = [\bar{L}_1, \bar{L}_2, \dots, \bar{L}_n] \quad (2)$$

When the radius is set to a value that is all-encompassing at every node (i.e., all nodes are always in the radius of influence), the RSP map simply assigns earlier path nodes with higher values and later nodes with lower values. An RSP map with a radius of r_2 (encompasses two neighboring path nodes) leads to an abstract depiction of the spatial intensity of the spatiotemporal temperature distribution, hence it has been utilized in this work to analyze correlations between it and post-print properties. It should be noted that a radius of r_2 will not yield the same results for different nodal discretization densities and hence is subject to its own tuning procedure.

In this study, the RSP map is applied on random Hamiltonian paths

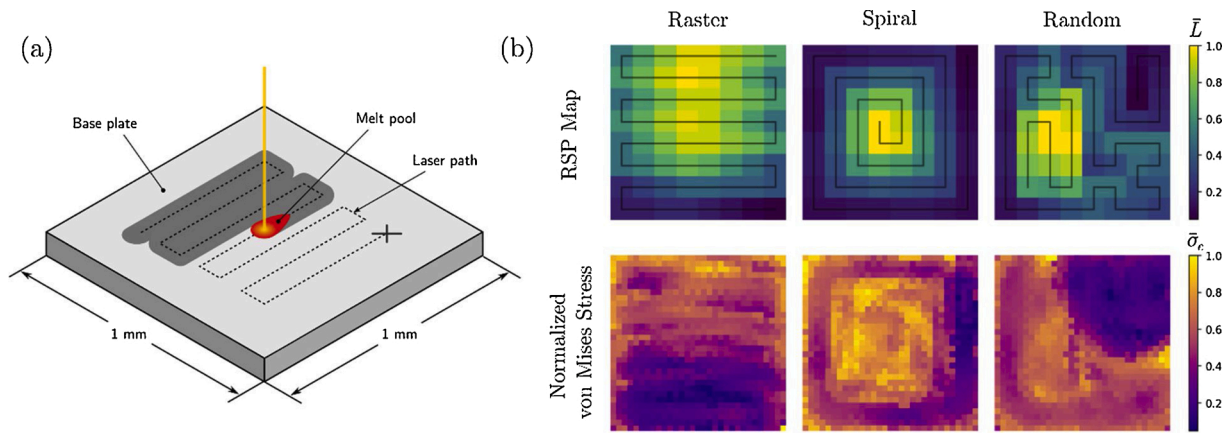


Fig. 2. (a) Depiction of the process being simulated. (b) Simulated normalized von Mises stress distributions and RSP maps of different paths.

that fill up a square grid. A Hamiltonian path is a path between two nodes of a graph, in this case, a square grid graph, which visits every other node in the graph. Hamiltonian paths can be generated on grid graphs using the backbite algorithm [17]. Hamiltonian paths will serve in this study as a source of variation in the RSP maps of different paths. It should be noted that there need not be a constraint on the continuity of a path in PBF processes; however, discontinuous paths such as the contour path shown in Fig. 1(a) are not considered in this study.

3. Simulation setup

In order to investigate the correlations between the RSP map and post-print properties, 10,000 random, 8 by 8, square grid Hamiltonian paths are generated and used in weakly coupled plane-strain thermoelastoplastic finite element simulations to obtain every path's corresponding von Mises stress distribution at the end of each print process (i. e., at room temperature). The von Mises distributions provided a good amount of distributive complexity which served the purposes of this study well.

In order to obtain as much data as possible, the simulations are setup with simplifying assumptions. These assumptions include, (1) Since only one 'layer' is being studied here, a 2D plane stress assumption is made in order to reduce computation times significantly. It is assumed that the anti-plane laser heat distribution is constant. (2) In PBF, the print bed (the base on top of which the powder is fused together) is the main heat sink in the process when compared to the heat loss due to convection and radiation. The 2D nature of the simulations here disallows for anti-plane heat conduction. Hence, this is artificially accommodated for in the formulation for the thermal part of the simulations. (3) Normally, powder layers are consolidated on top of the print bed (or a previously consolidated area). After solidification the print bed imposes displacement constraints on the layer. These constraints are ignored in this study. (4) The entire domain is set up as a homogeneous solid. Hence, material properties, such as the thermal conductivity, density, and specific heat capacity, are not modeled to capture particle behaviors and are only dependent on temperature. (5) Melt pool fluid dynamics are completely ignored. In order to capture the deformation of freshly solidified material the yield stress at melting temperatures is set to be three orders of magnitude below the yield stress of the material at room temperature to allow for increased material flow. Simulating PBF processes accurately is a prominent research topic as the process is incredibly complex, involving four states of matter all interacting with one another at different scales [18–20]. Nevertheless, the presumption that the final state of this simulation is deterministic given a set of initial process parameters and a material model, regardless of its accuracy, allows for investigative space.

3.1. Thermal model

As depicted in Fig. 2(a), every simulation involves a 1 mm by 1 mm surface area with a 0.1 mm powder layer thickness which is then consolidated using a laser with a diameter of 100 microns. There is a 10 % area overlap in between each laser path which is commonly done in PBF processes to assure proper consolidation. The speed of the laser beam is held constant over the path at 1 m/s with a power of 40 W. The governing equations for the thermal simulations are,

$$\rho C_p \dot{\theta} = \nabla \cdot (K \nabla \theta) + Q + B \tag{3}$$

where θ , ρ , C_p , and K are the temperature, density, specific heat capacity and thermal conductivity of the base plate material. Q is the volumetric 2D Gaussian heat source distribution which translates over the surface along the laser path and B is the conductive heat loss to the print bed.

$$Q(x, t) = \frac{P}{\pi R^2 h} \exp\left(-\frac{1}{R^2} |x - x_p(t)|^2\right) \tag{4}$$

where x_p is the position of the laser at time t as per the laser path, R is the radius of the laser, h is the thickness of the base plate, and P is the power of the laser. B is derived by performing a finite difference approximation of the second order derivative of the temperature in the out-of-plane direction (see assumption (2)),

$$B(\theta) = K \frac{\partial^2 \theta}{\partial z^2} \approx K \frac{2(\theta - \theta_b)}{h^2} \tag{5}$$

where h is 0.1 mm (approximate powder layer thickness) and θ_b is the temperature of the print bed and is held constant at room temperature since the print bed is usually significantly more massive than the laser heated material. No thermal other boundary conditions were imposed. To capture the temperature dependence and the effect of the latent heat of fusion, the apparent heat capacity method [21,22] is used where C_p is modeled as,

$$C_p(\theta) = C_n(\theta) + C_{ap}(\theta) \tag{6}$$

where,

$$C_n(\theta) = C_s + \frac{C_l - C_s}{2} \left(1 + \tanh\left(8 \frac{\theta - \theta_m}{\theta_2 - \theta_1}\right)\right) \tag{7}$$

$$C_{ap}(\theta) = \frac{2L}{\theta_2 - \theta_1} \cos^2\left(\pi \frac{\theta - \theta_m}{\theta_2 - \theta_1}\right) \tag{8}$$

and where C_n is the function capturing purely the temperature dependence and C_{ap} is the apparent heat capacity capturing the behavior of latent heat. θ_1 and θ_2 define lower and upper bounds of the temperature

range wherein latent heat effects take place.

In Eq. (9) the weak linearized form is obtained (prior to the finite element discretization) to solve the heat equation. The residual S_0^i is derived from Eq. (3) through the implementation of a Crank-Nicolson time integration scheme. This residual is then used in a Newton-Raphson iterative scheme to solve for θ^i , the temperature at the i^{th} timestep (note that superscripts in Eq. (9) alone denote time iterations).

$$S_0(\theta^i) = \int_{\Omega} \rho C_p (\theta^i - \theta^{i-1}) \theta_v dx - \Delta t \left(\frac{1}{2} \int_{\Omega} K ((\nabla \theta^i + \nabla \theta^{i-1}) \cdot \nabla \theta_v) dx + \int_{\Omega} Q(x, t) \theta_v dx + \frac{1}{2} \int_{\Omega} (B(\theta^i) + B(\theta^{i-1})) \theta_v dx \right) \quad (9)$$

where θ_v is the test function.

3.2. Mechanical model

The mechanical material model here is taken to exhibit linear isotropic elasticity and perfect rate-independent plasticity. The material is assumed to behave quasi-statically under induced thermal strains. The strain is additively decomposed into its elastic (ϵ_e), plastic (ϵ_p), and thermal (ϵ_θ) components,

$$\epsilon = \epsilon_e + \epsilon_p + \epsilon_\theta, \quad \epsilon_\theta = \alpha \Delta \theta \mathbf{I} \quad (10)$$

where α is the linear thermal expansion coefficient, $\Delta \theta$ is the temperature change and \mathbf{I} is the identity tensor. The balance of linear momentum is solved for,

$$\nabla \cdot \sigma = 0 \quad (11)$$

where σ is the Cauchy stress tensor. The von Mises yield criterion is used.

$$f = |\tau| - \sqrt{2}k \leq 0, \quad |\tau| = \text{tr}(\tau : \tau) \quad (12)$$

where $\tau = \text{dev}(\sigma)$ and k is the yield shear stress defined as,

$$k(\theta) = k_0 \varphi^{\frac{\theta - \theta_0}{\theta_m - \theta_0}}, \quad \varphi \ll 1 \quad (13)$$

where φ is the reduction factor, k_0 is the room temperature yield stress, and θ_0 is the initial temperature of the base plate, and θ_m is the melting temperature of the material. Note that this is not necessarily the best way to approach the flow of material in the melt pool; however it is computationally inexpensive, simple to implement, and effective in producing sufficient material flow for plastic strain development. The plastic flow is governed by the following flow rule,

$$\dot{\epsilon}_p = \dot{\lambda} \frac{\tau}{|\tau|} = \dot{\lambda} n \quad (14)$$

where $\dot{\lambda}$ is the plastic strain evolution rate.

The following weak form of Eq. (11) is obtained,

$$S_\sigma(u) = \int_{\Omega} \epsilon_v : (\sigma - \mathbb{E} : \epsilon_\theta) dx = 0 \quad (15)$$

where S_σ is the residual with respect to u , the discontinuous displacement field, and ϵ_v is the test function and, \mathbb{E} is the fourth rank elasticity tensor defined as,

$$\mathbb{E} = K \mathbf{I} \otimes \mathbf{I} + 2G \mathbf{I}_{\text{dev}} \quad (16)$$

where K is the bulk modulus, G is the shear modulus and, $\mathbf{I}_{\text{dev}} : \mathbf{A} = \text{dev}(\mathbf{A})$ for any second order tensor \mathbf{A} . The weak form is then linearized using the Newton-Raphson iterative scheme and the return map algorithm is then implemented to track and solve for plastic strains [25].

All simulation parameters, including thermoelastoplastic properties, laser parameters, the finite element mesh, and the simulated timestep,

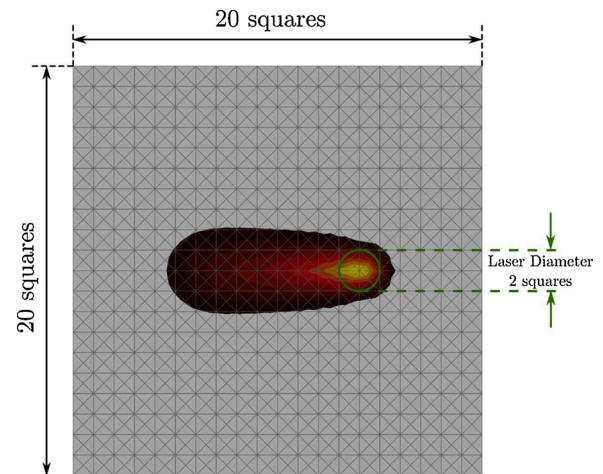


Fig. 3. Finite element mesh depiction. Each square contains four triangular elements. Red shades represent thermal profile immediate to laser spot (green circle) after a horizontal scan from left to right. (For interpretation of the references to colour in this figure legend, the reader is referred to the web version of this article).

Table 1
Description of NN properties.

Layer	Number of Neurons	Activation Function
Input	64	ReLU
First Hidden	64	ReLU
Second Hidden	225	ReLU
Output	961	Sigmoid

were kept constant across all simulations to measure correlations between the RSP map and residual stress profiles derived from variations in scan paths. It should be noted that due to the nonlinear nature of the equations, inconsistencies may arise from numerical errors associated with convergence characteristics of the iterative numerical implementation which can be influenced by the type of simulated scan path.

There are many different ways to go about the model formulations, finite element implementation, time integration schemes, and meshing however for the sake of brevity we refer the reader to [23–28] for more detailed discussions. To mention a few properties of the finite element implementation, triangular linear elements were used for the thermal mesh while triangular quadratic elements were used for the mechanical mesh. The same number of elements were used for both the thermal and mechanical meshes, with a mesh density of 2 triangular element per laser radius as shown in Fig. 3. An inhouse software is developed to carry out the calculations using FEniCs, an automated finite element solver package [29].

4. Neural network setup

Considering the complexity of the physics involved in mAM, machine learning stands out as an attractive investigative tool owing to its ability to efficiently extract correlations from chaotic datasets which provides avenues for deeper understandings [30–35]. Neural networks (NN), or artificial neural networks, are mathematical models that map input data to output data through the utilization of artificial neurons connected in certain ways. The Feedforward NN, used in this work, is a type of NN in which neurons are connected in a noncyclical manner.

The neural network used here consists of four densely connected layers, the input layer which takes as its input the vectorized form of the RSP map (\bar{L}), the output layer which outputs the vectorized von Mises stress profile of 961 points (making up the 31 by 31 stress profile) and, two hidden layers. The layers and their activation functions are shown in

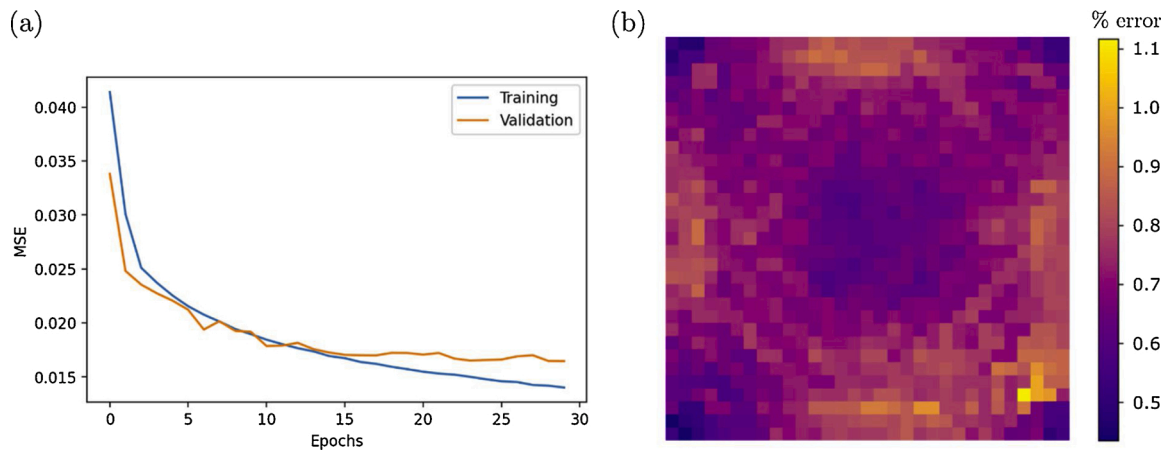


Fig. 4. (a) NN training and validation MSE error plot. Epochs are training iterations associated with the backpropagation algorithm where one iteration involves algorithmically ‘passing’ through the training data once. (b) The average percentage error map of the normalized residual stress predictions of test data.

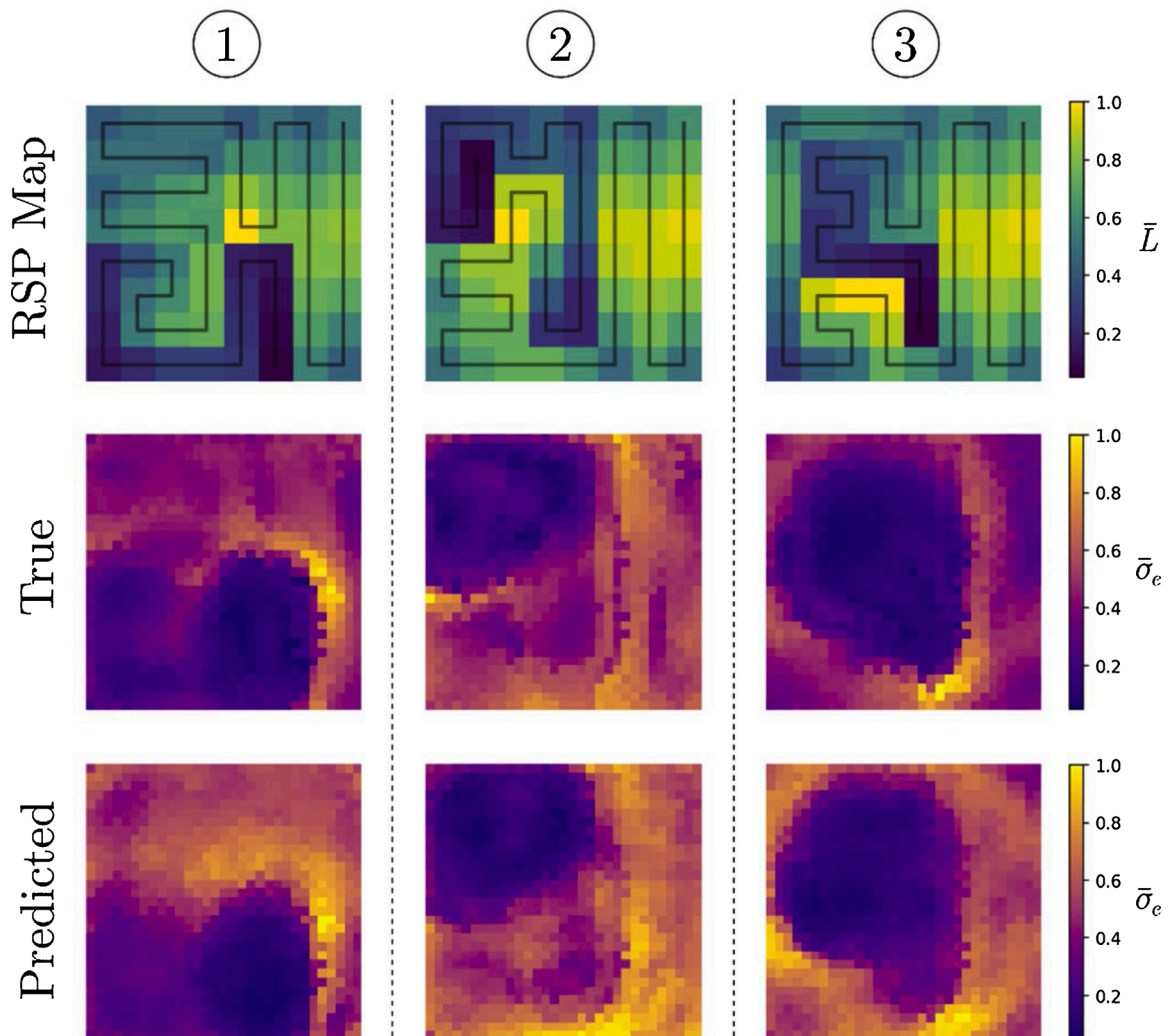


Fig. 5. Prediction performance of neural network trained on the RSP maps. Each column represents the (test) RSP map, normalized true simulated von Mises residual stress distribution, and normalized predicted von Mises residual stress distribution of a specific path.

Table 1. The nodes in the input and hidden layers are assigned ReLU activation functions while the output nodes are assigned sigmoidal activation functions. The output range of sigmoidal functions is [0, 1] which is then linearly scaled up to a range from [0, σ_0] to represent the

final stress state, where σ_0 is the von Mises yield stress at room temperature. The backpropagation algorithm is used to optimize the weights and biases of the nodes and train the network. The structure of the NN was designed by balancing prediction accuracy and training

speed.

5. Results and discussion

The NN has a total of 240,131 trainable parameters (total number of weights and biases) trained on a data set of 10,000 simulations. The data was split into 7500 training, 1250 validating and 1250 testing data points. Fig. 4(a) shows the training and validation mean squared error (MSE) of the neural network over the training process. In order to better investigate the predictive error, an average percentage error map was made by averaging over every test prediction's individual error map. A prediction's error map $[\bar{\sigma}_{\text{err}}]$ is attained by simply evaluating the difference between the predicted $[\bar{\sigma}_{\text{pred}}]$ and simulated $[\bar{\sigma}_{\text{sim}}]$ von Mises stress distributions.

$$[\bar{\sigma}_{\text{err}}]_{\text{avg}} = \frac{1}{N} \sum_i [\bar{\sigma}_{\text{err}}]_i = \frac{1}{N} \sum_i \left(\frac{\text{abs}([\bar{\sigma}_{\text{pred}}]_i - [\bar{\sigma}_{\text{sim}}]_i)}{[\bar{\sigma}_{\text{sim}}]_i} \right) \quad (17)$$

In other words, every pixel on the average error map is the global average error of that pixel's prediction. The maximum average percent error of any pixel is 1.1 % as can be seen in Fig. 4(b).

The NN is able to predict a significant amount of detail including immediate spatial von Mises stress transitions from smaller to larger \bar{L} values. The predictions of the NN can be seen in Fig. 5, where three new test paths are generated and used to predict their von Mises stress distributions at room temperature. In Fig. 5, it can be seen that the NN learns that areas corresponding to the end of the paths, (i.e., smaller \bar{L} values) have smaller von Mises stress values and vice versa.

A powerful attribute of the RSP map is that it is not constrained to the regularity of the scan strategies studied here. The RSP map is applicable to any strategy with any level of nodal discretization. Furthermore, in this study the speed of the laser is held constant however it too could be varied and analyzed. A spatially varying laser velocity would manifest itself in the RSP map through the time difference in Eq. (1). We aim to investigate this in future work. The RSP map can even be applied with techniques such as island scanning, where patches of spaced-out areas are sequentially scanned over for heat control. Each island could be considered as a node in an *island-scale* RSP map which could allow for macroscopic applicability. One promising advancement of this work would be the inverse problem, where optimal RSP maps, and consequently optimal strategies, for any given area are searched for. Although this is would be a speculative suggestion, the RSP map can potentially be correlated with other types of defects too such as porosity and surface roughness since the literature contains works correlating laser scan patterns to these defects.

6. Conclusions

It has been demonstrated that there are attainable correlations between the proposed laser scan strategy descriptor, the RSP map, and the outcomes of the simulated von Mises residual stress distribution at the end of a single layer pass. A neural network is trained to obtain the correlations and perform the predictions which are inspiringly accurate, instilling confidence in the RSP map as a descriptor. This provides hope for the methodology to be extended to higher accuracy predictions at larger scales and for various print properties. The RSP map shows promising applicability in mAM process planning where laborious trial-and-error procedures and expensive computational simulations are relied upon. It is envisioned that this method will allow for quick and easy prognoses of process parameters in order to prevent expensive failures and push for the further proliferation of mAM technologies.

Declaration of Competing Interest

The authors report no declarations of interest.

Acknowledgements

This work used the Extreme Science and Engineering Discovery Environment (XSEDE) Bridges system, which is supported by National Science Foundation grant number ACI-1548562. Additionally, the authors acknowledge support from 3M and the Savio computational cluster resource provided by the Berkeley Research Computing program.

References

- [1] Joshi SC, Sheikh AA. 3D printing in aerospace and its long-term sustainability. *Virtual Phys Prototyp* 2015;10:175–85. <https://doi.org/10.1080/17452759.2015.1111519>.
- [2] Alcácer V, Cruz-Machado V. Scanning the industry 4.0: a literature review on technologies for manufacturing systems. *Eng Sci Technol Int J* 2019;22:899–919. <https://doi.org/10.1016/j.jestch.2019.01.006>.
- [3] Jin Z, Zhang Z, Demir K, Gu GX. Machine learning for advanced additive manufacturing. *Matter* 2020;3:1541–56.
- [4] Dilberoglu UM, Gharehpapagh B, Yaman U, Dolen M. The role of additive manufacturing in the era of industry 4.0. *Procedia Manuf* 2017;11:545–54. <https://doi.org/10.1016/j.promfg.2017.07.148>.
- [5] Gisario A, Kazarian M, Martina F, Mehrpouya M. Metal additive manufacturing in the commercial aviation industry: a review. *J Manuf Syst* 2019;53:124–49. <https://doi.org/10.1016/j.jmsy.2019.08.005>.
- [6] Zhang Z, Demir KG, Gu GX. Developments in 4D-printing: a review on current smart materials, technologies, and applications. *Int J Smart Nano Mater* 2019: 1–20.
- [7] Sireesha M, Lee J, Kranthi Kiran AS, Babu VJ, Kee BBT, Ramakrishna S. A review on additive manufacturing and its way into the oil and gas industry. *RSC Adv* 2018; 8:22460–8. <https://doi.org/10.1039/c8ra03194k>.
- [8] Tofail SAM, Koumoulos EP, Bandyopadhyay A, Bose S, O'Donoghue L, Charitidis C. Additive manufacturing: scientific and technological challenges, market uptake and opportunities. *Mater Today* 2018;21:22–37. <https://doi.org/10.1016/j.matod.2017.07.001>.
- [9] Gu GX, Takaffoli M, Buehler MJ. Hierarchically enhanced impact resistance of bioinspired composites. *Adv Mater* 2017;29:1700060.
- [10] Frazier WE. Metal additive manufacturing: a review. *J Mater Eng Perform* 2014;23: 1917–28. <https://doi.org/10.1007/s11665-014-0958-z>.
- [11] Herzog D, Seyda V, Wycisk E, Emmelmann C. Additive manufacturing of metals. *Acta Mater* 2016;117:371–92. <https://doi.org/10.1016/j.actamat.2016.07.019>.
- [12] Kirka MM, Nandwana P, Lee Y, Dehoff RR. Solidification and solid-state transformation sciences in metals additive manufacturing. *Scr Mater* 2017;135: 130–4. <https://doi.org/10.1016/j.scriptamat.2017.01.005>.
- [13] Arisoy YM, Criales LE, Özel T, Lane B, Moylan S, Donmez A. Influence of scan strategy and process parameters on microstructure and its optimization in additively manufactured nickel alloy 625 via laser powder bed fusion. *Int J Adv Manuf Technol* 2016;90:1393–417. <https://doi.org/10.1007/s00170-016-9429-z>.
- [14] Rashid R, Masood SH, Ruan D, Palanisamy S, Rahman Rashid RA, Brandt M. Effect of scan strategy on density and metallurgical properties of 17-4PH parts printed by Selective Laser Melting (SLM). *J Mater Process Technol* 2017;249:502–11. <https://doi.org/10.1016/j.jmatprotec.2017.06.023>.
- [15] Levkulich NC, Semiatin SL, Gockel JE, Middendorf JR, DeWald AT, Klingbeil NW. The effect of process parameters on residual stress evolution and distortion in the laser powder bed fusion of Ti-6Al-4V. *Addit Manuf* 2019;28:475–84. <https://doi.org/10.1016/j.addma.2019.05.015>.
- [16] Lee YS, Kirka MM, Ferguson J, Paquit VC. Correlations of cracking with scan strategy and build geometry in electron beam powder bed additive manufacturing. *Addit Manuf* 2020;32. <https://doi.org/10.1016/j.addma.2019.101031>.
- [17] Mansfield ML. Monte Carlo studies of polymer chain dimensions in the melt. *J Chem Phys* 1982;77:1554–9. <https://doi.org/10.1063/1.443937>.
- [18] Khairallah SA, Anderson AT, Rubenchik A, King WE. Laser powder-bed fusion additive manufacturing: physics of complex melt flow and formation mechanisms of pores, spatter, and denudation zones. *Acta Mater* 2016;108:36–45. <https://doi.org/10.1016/j.actamat.2016.02.014>.
- [19] Panwisawas C, Tang YT, Reed RC. Metal 3D printing as a disruptive technology for superalloys. *Nat Commun* 2020;11:2327. <https://doi.org/10.1038/s41467-020-16188-7>.
- [20] Bidare P, Bitharas I, Ward R, Attallah M, Moore AJ. Fluid and particle dynamics in laser powder bed fusion. *Acta Mater* 2018;142:107–20.
- [21] Foteinopoulos P, Papacharalampopoulos A, Stavropoulos P. On thermal modeling of Additive Manufacturing processes. *Cirp J Manuf Sci Technol* 2018;20:66–83. <https://doi.org/10.1016/j.cirpj.2017.09.007>.
- [22] Hu H, Argyropoulos SA. Mathematical modelling of solidification and melting: a review. *Modelling and simulation in materials science and engineering*, 4; 1996. p. 371.
- [23] Gouge M, Denlinger E, Irwin J, Li C, Michaleris P. Experimental validation of thermo-mechanical part-scale modeling for laser powder bed fusion processes. *Addit Manuf* 2019;29. <https://doi.org/10.1016/j.addma.2019.06.022>.
- [24] Gouge M, Michaleris P, Denlinger E, Irwin J. The finite element method for the thermo-mechanical modeling of additive manufacturing processes. 2018.
- [25] Simo JC, Taylor RL. Consistent tangent operators for rate-independent elastoplasticity. *Computer methods in applied mechanics and engineering*, 48; 1985. p. 101–18.

- [26] Carraturo M, Jomo J, Kollmannsberger S, Reali A, Auricchio F, Rank E. Modeling and experimental validation of an immersed thermo-mechanical part-scale analysis for laser powder bed fusion processes. *Addit Manuf* 2020;36:101498. <https://doi.org/10.1016/j.addma.2020.101498>.
- [27] Zohdi TI. Modeling and simulation of laser processing of particulate-functionalized materials. *Archives of computational methods in engineering*, 24; 2015. p. 89–113. <https://doi.org/10.1007/s11831-015-9160-1>.
- [28] Zohdi TI. Ultra-fast laser-patterning computation for advanced manufacturing of powdered materials exploiting knowledge-based heat-kernels. *Comput Methods Appl Mech Eng* 2019;343:234–48. <https://doi.org/10.1016/j.cma.2018.08.040>.
- [29] Automated solution of differential equations by the finite element method. 2012.
- [30] Chen CT, Gu GX. Generative deep neural networks for inverse materials design using backpropagation and active learning. *Adv Sci* 2020;1902607.
- [31] Begg R, Kamruzzaman J. A machine learning approach for automated recognition of movement patterns using basic, kinetic and kinematic gait data. *J Biomech* 2005;38:401–8.
- [32] Yang C, Kim Y, Ryu S, Gu GX. Prediction of composite microstructure stress-strain curves using convolutional neural networks. *Mater Des* 2020;189:108509.
- [33] Musil F, De S, Yang J, Campbell JE, Day GM, Ceriotti M. Machine learning for the structure–energy–property landscapes of molecular crystals. *Chem Sci* 2018;9: 1289–300.
- [34] Jin Z, Zhang Z, Ott J, Gu GX. Precise localization and semantic segmentation detection of printing conditions in fused filament fabrication technologies using machine learning. *Addit Manuf* 2020;101696.
- [35] Pilia G, Wang C, Jiang X, Rajasekaran S, Ramprasad R. Accelerating materials property predictions using machine learning. *Sci Rep* 2013;3.